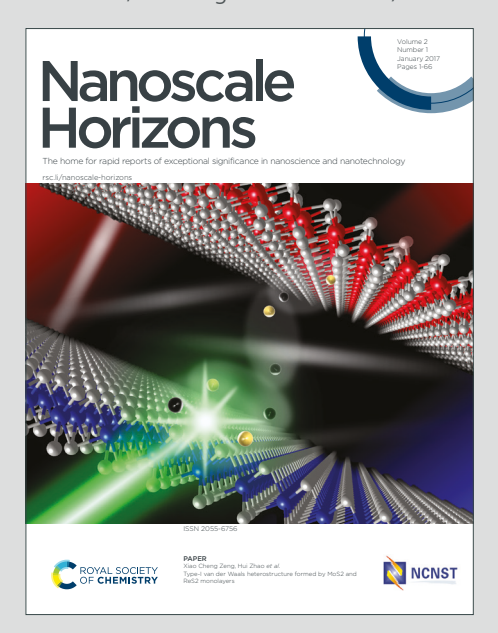
Nanoscale Horizons



The home for rapid reports of exceptional significance in nanoscience and nanotechnology

Accepted Manuscript

This article can be cited before page numbers have been issued, to do this please use: A. Alowasheeir, Md. I. U. Hoque, X. Xu, S. Donne, Y. Bando, S. M. Alshehri, T. Ahamad, Md. S. A. Hossain, Y. Yamauchi, N. Amiralian, D. Jiang and Y. Asakura, *Nanoscale Horiz.*, 2025, DOI: 10.1039/D5NH00306G.



This is an Accepted Manuscript, which has been through the Royal Society of Chemistry peer review process and has been accepted for publication.

Accepted Manuscripts are published online shortly after acceptance, before technical editing, formatting and proof reading. Using this free service, authors can make their results available to the community, in citable form, before we publish the edited article. We will replace this Accepted Manuscript with the edited and formatted Advance Article as soon as it is available.

You can find more information about Accepted Manuscripts in the <u>Information for Authors</u>.

Please note that technical editing may introduce minor changes to the text and/or graphics, which may alter content. The journal's standard <u>Terms & Conditions</u> and the <u>Ethical guidelines</u> still apply. In no event shall the Royal Society of Chemistry be held responsible for any errors or omissions in this Accepted Manuscript or any consequences arising from the use of any information it contains.



View Article Online DOI: 10.1039/D5NH00306G

New Concept Statement

Capacitive deionization (CDI) is a promising desalination technology due to its low energy consumption and eco-friendly nature. However, the performance of CDI electrodes remains a critical challenge, particularly in achieving high salt adsorption capacity, fast ion transport, and long-term cycling stability. In this study, we introduce a new class of nanocomposites derived from nanocellulose and reduced graphene oxide (rGO), where nanocellulose functions as a structural spacer to prevent rGO restacking and enhance pore accessibility. By employing three distinct nanocellulose morphologies—cellulose nanofibers (CNF), long cellulose nanocrystals (CNC-L), and short cellulose nanocrystals (CNC-S)—we systematically control the structure and porosity of the resulting composites. Among these, CNC-L/rGO delivers an exceptional CDI performance, achieving a Na⁺ adsorption capacity of 45.67 mg g⁻¹ and outstanding cycling durability. This work represents the first application of nanocellulose-derived carbon/rGO nanocomposites for CDI, offering a sustainable and tunable material platform. The strategic integration of renewable nanocellulose with conductive carbon architectures opens a new avenue in designing high-performance CDI electrodes. These findings not only advance the understanding of hierarchical carbon composite design but also offer practical insight for scalable desalination technologies targeting freshwater scarcity.

Synthesis of Carbon Nanocomposites Consisting of Nanocellulose-

1

2

3

40

<u>ā</u>1

papeolumod 5

505

16.0ktober 2

hed 00

28

29

30

Derived Carbon Fibers and Reduced Graphene Oxide for High-

Performance Captive Deionization

5	Azhar Alowasheeir, ⁺¹ Md. Ikram Ul Hoque, ^{+2,3} Xingtao Xu, ⁴ Scott W. Donne, ³ Yoshio Bando, ^{5,6}
6	Saad M. Alshehri, ⁶ Tansir Ahamad, ⁶ Md. Shahriar A. Hossain, ^{2,7} Yusuke Yamauchi, ^{1,2}
7	Nasim Amirallian, ^{2*} Dong Jiang, ^{1,2*} and Yusuke Asakura ^{1*}
8	

- ¹ Department of Materials Process Engineering, Graduate School of Engineering, Nagoya University, Nagoya 464-8603, Japan.
- ² Australian Institute for Bioengineering and Nanotechnology (AIBN), The University of Queensland, Brisbane, Queensland 4072, Australia.
- ³ Discipline of Chemistry, The University of Newcastle, University Drive, Callaghan, NSW 2308, Australia.
- ⁴ Marine science and technology college, Zhejiang Ocean University, Zhoushan, China.
- ⁵ School of Mechanical and Mining Engineering, Faculty of Engineering, Architecture, and Information Technology (EAIT), The University of Queensland, Brisbane, QLD, 4072, Australia.
- ⁶ Chemistry Department, College of Science, King Saud University, Riyadh 11451, Saudi Arabia.
- ⁷ Australian Institute for Innovative Materials, University of Wollongong, North Wollongong 2500, Australia.

Abstract: Several types of nanocellulose-derived carbon/reduced graphene oxide (rGO) nanocomposites are synthesized using three nanocellulose types: cellulose nanofibers (CNF), long cellulose nanocrystals (CNC-L), and short cellulose nanocrystals (CNC-S). The nanocomposites achieve a large surface area due to the small

- 23 nanocellulose fibers acting as spacers. For the capacitive deionization (CDI) test, the CNC-L/rGO is selected
- 24 and compared with the rGO prepared without nanocelluloses. It achieves a high sodium ion adsorption capacity
- 25 of 45.67 mg g⁻¹ and a high salt adsorption capacity of 57.08 mg g⁻¹ at a NaCl concentration of 2,000 mg L⁻¹.
- 26 Excellent stability and performance are also confirmed across varying saline concentrations. These outstanding
- 27 properties make the CNC-L/rGO a promising electrode material for efficient and sustainable water desalination.

946 E

Freshwater scarcity, a pressing global challenge exacerbated by climate change, overpopulation, water pollution,

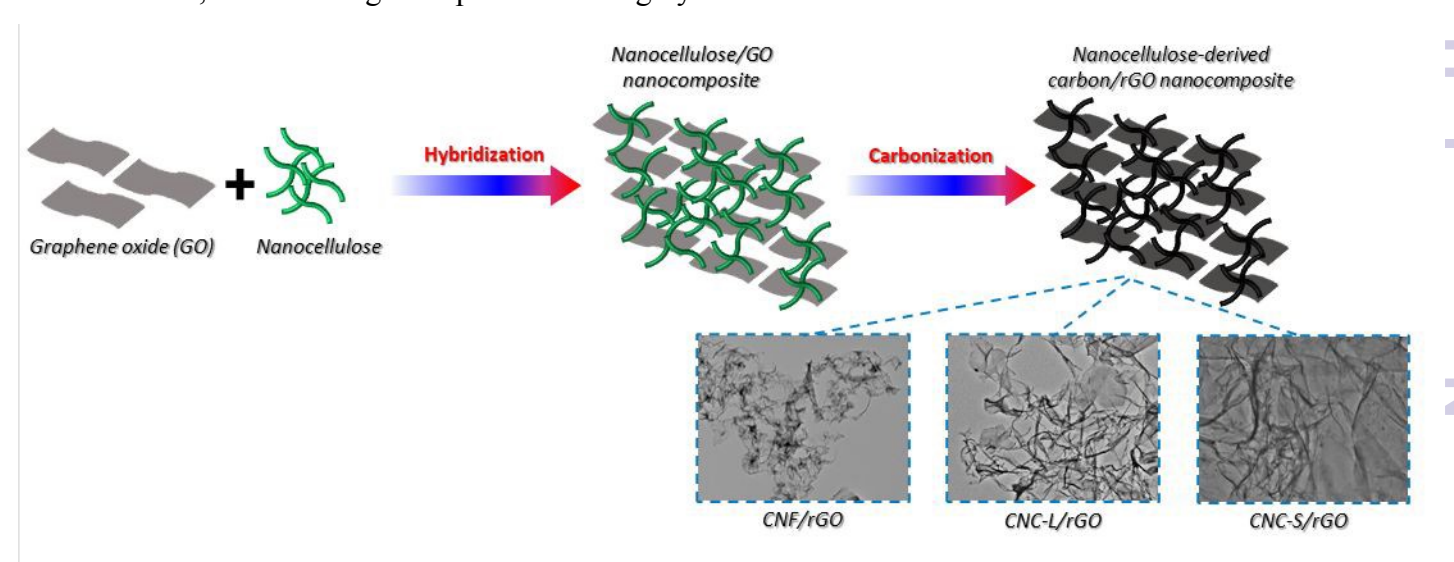
31 1. Introduction:

and unsustainable water resource utilization, demands innovative solutions. 1,2 Desalination, 41/2/1910/06/35/0f removing salts from saltwater or brackish water, presents a promising avenue for producing clean, fresh water. There are several desalination methods, such as thermal desalination and membrane-based techniques. Thermal desalination utilizes heat to evaporate water and separate it from salts, while membrane-based techniques, such as reverse osmosis and electrodialysis, employ semi-permeable membranes to filter out salts. 1,3 In these desalination processes, however, high energy consumption, substantial costs, and potential environmental impacts pose limitations for large-scale freshwater production. ⁴⁻⁶ Recently, capacitive deionization (CDI) has garnered significant interest among researchers worldwide. 1,2,4,7-9 The CDI operates at a low voltage between two electrodes, where ions from an aqueous solution are adsorbed via the electrical double layer (EDL) 42 mechanism. This process does not generate harmful byproducts. Instead, energy can be recovered during the ₹3 release of counter ions and electrode regeneration by simply reversing the electrode polarity. Consequently, CDI 24 is considered a promising desalination technology due to its cost-effectiveness, high energy efficiency, and s environmentally friendly attributes compared to conventional desalination methods.

The efficiency and capacity of CDI technology are strongly dependent on the electrode properties. To 47 date, a wide range of nanoporous materials, including carbon-based materials, metal-organic frameworks № (MOFs), covalent-organic frameworks (COFs), ¹⁰ polymers, and metal oxides, ¹¹ have been investigated for CDI applications. 1,2,8,12-14 Among these, carbon-based materials, such as carbon aerogels, 15 activated carbon, 16 carbon nanotubes (CNTs)-based composites, ¹⁷ nanostructured carbon ¹⁸ and other graphene-based materials, ¹⁹ र्दे। are favored due to their desirable properties, including high electrical conductivity, good chemical stability, and $\frac{5}{2}$ ease of surface modification, coupled with economic benefits such as low synthesis cost and abundance. ^{1,12} The CDI's electrochemical functions, mechanisms, and principles are closely related to those of supercapacitors. Therefore, physicochemical parameters that enhance supercapacitor performance are similarly effective in the CDI. 1,12,20,21 55

Graphene-based nanocomposites have shown promise in various electrochemical applications. ^{22,23} 56 Graphene plays a vital role in these nanocomposites, enhancing electrical conductivity and physicochemical stability. However, graphene nanosheets themselves are seriously stacked to each other, reducing the exposed active surface area. Self-assembly of graphene nanosheets can yield porous nanoarchitecture by incorporating with CNTs or crosslinking with polymers. ¹⁹ Nanocelluloses that can be widely obtained from natural cellulose sources exhibit one-dimensional (1D) morphologies having uniform diameters ranging from 10-100 nm and lengths from 100 nm to several microns. ²²⁻²⁵ By using different types of nanocelluloses, carbon materials with varying morphologies, textures, etc., can be designed in a desired manner. ^{22,23,26} Therefore, graphene-based nanocomposites with nanocelluloses as spacers are expected to retain high exposed surface area, and they are 65 expected to be a promising candidate for CDI applications. To the best of our knowledge, however, the 66 application of nanocellulose-derived carbon/rGO nanocomposites to CDI has not been previously reported. In 67 this study, we report the synthesis of nanocellulose-derived carbon/rGO nanocomposites using three types of 68 nanocellulose produced via different treatments, each exhibiting unique distinctions in morphologies, size, and properties: (1) CNF (cellulose nanofibril) with a width of 2–50 nm and a length of 1–3 µm (the most extended 70 length among the types), (2) CNC-L (long cellulose nanocrystal) with a width of 10–20 nm and a leave the property of 500– 1000 nm (shorter than CNF but longer than CNC-S), and (3) CNC-S (short cellulose nanocrystal) with a width of 10–20 nm and a length of 300–500 nm (the shortest length) (Scheme 1). Importantly, in this design, nanocellulose acts not only as a space but also as a morphology-regulating agent. Specifically, differences in fiber length and crystallinity among CNF, CNC-L, and CNC-S allow for precise tuning of the resulting pore architectures and conductive pathways. The CNC-L forms an extended conductive network and introduces a 76 larger mesoporous structure, while the CNC-S forms a denser and more compact structure. This structural tunability allows for effective control over ion transport dynamics in the CDI system. ²⁷ Furthermore, the incorporation of appropriately-sized nanocellulose spacers suppresses the restacking of the rGO layers and enhances ion accessibility.²⁸

In parallel, recent studies have emphasized the importance of architecturally-engineered electrodes that \$1 integrate hierarchical porosity, structural stability, and well-defined ion transport pathways to advance CDI 82 performance.²⁹ Our design strategy is well aligned with this emerging direction. The concept of using bioderived nanoscale spacers to regulate the structure of two-dimensional materials can be extended to other layered \$4 materials such as MXenes, layered double hydroxides, and transition metal dichalcogenides. We \$5 comprehensively characterize the resulting nanocomposites to determine their physicochemical properties, \$\frac{1}{28}6\$ including morphologies, textures, surface areas, pore size distributions, etc. The synthesized nanocomposites are then used to fabricate electrodes for a CDI device under controlled conditions (Fig. S1), enabling us to §8 systematically study and evaluate the impact of nanocelluloses on the CDI performance. Our nanocomposite demonstrates remarkable performance in the CDI applications in comparison with rGO prepared without nanocelluloses, underscoring their potential as highly efficient materials for water desalination.



92 **Scheme 1.** Synthesis strategy of nanocellulose-derived carbon/rGO nanocomposites prepared with graphene 93 oxide (GO) sheets and nanocellulose as the starting precursors.

95 2. Results and Discussion:

\$0

91

94

146

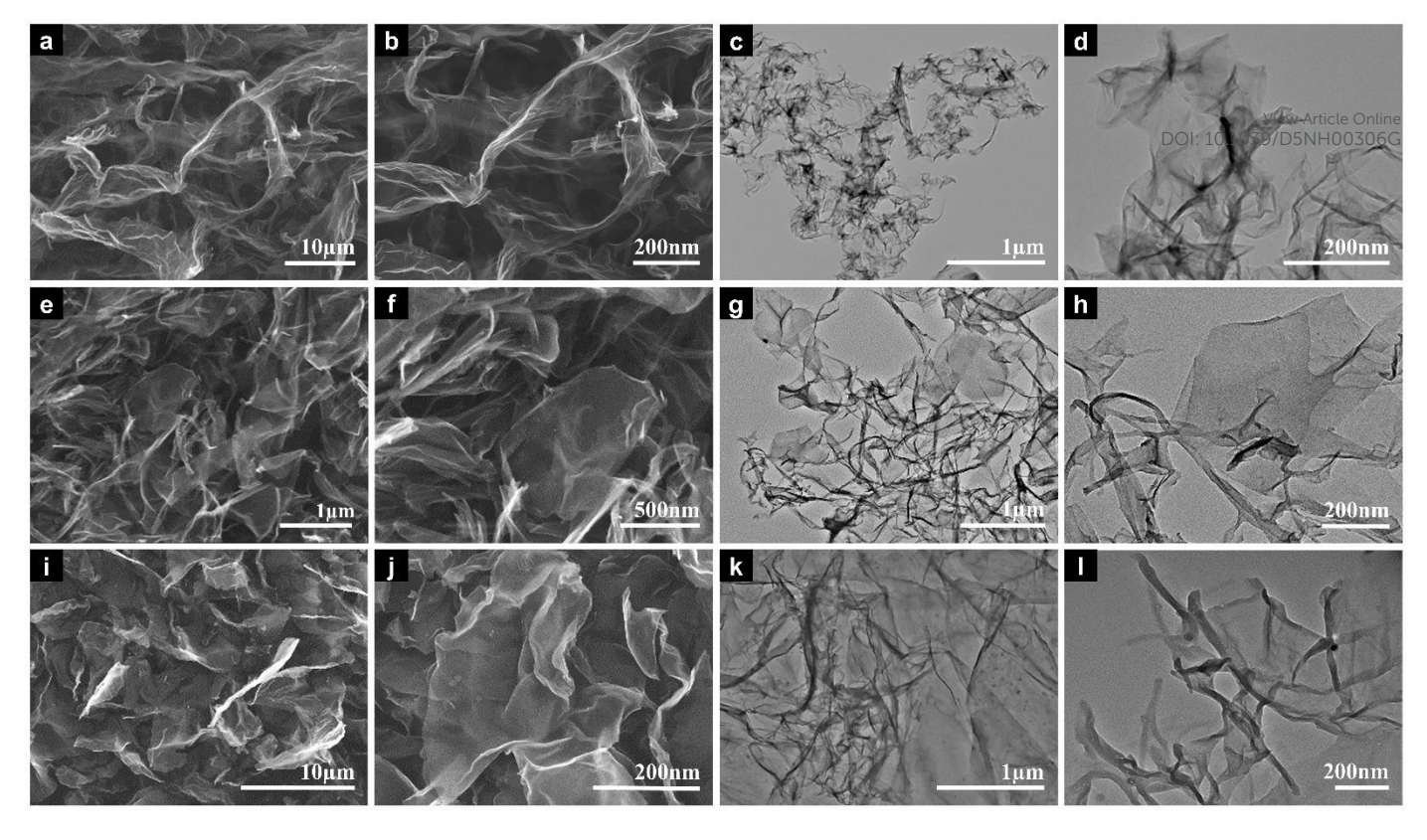
carbon/rGO nanocomposites.

96 The preparation process of the nanocellulose-derived carbon/rGO nanocomposites is illustrated in **Scheme 1**. The GO nanosheet precursor, synthesized using Hummers' method, exhibited a 2D crumpled sheet-like structure. 98 Nanocelluloses were incorporated into this structure through a self-assembly approach, facilitated by the functional groups present on both GO and nanocellulose surfaces (e.g., C-O, C=O, and hydroxyl (-OH) groups). ¹⁰ These functional groups promoted interactions through ionic interactions and/or hydrogen bonding via -OH groups. The precursor mixture, a brownish-black nanocellulose/GO nanocomposite, was obtained by flash freezing the suspension in liquid nitrogen, followed by drying at low pressure using a freeze dryer. Finally, the

103 powder was carbonized under nitrogen flow at 600 °C for 8 hours to produce the nanocellulose-derived

The three different types of nanocellulose used in this study are shown in TEM images in Fig. S2. CNF 106 (Fig. S2a) is produced via the mechanical treatment of sugarcane bleached pulp through a high-pressure 107 homogenizer. They consist of a combination of high-aspect-ratio individual fibers and their bundles. The surface 198 of these fibers is rich in hydroxyl groups, which bond through van der Waals forces, causing cellulose chains to 19 stack and form elementary fibrils or nanofibrils. 30,31,32 CNC-L, derived from sugarcane bleached pulps mild 130 sulfuric acid treatment, also shows an elongated, flexible structure but with shorter fiber lengths (**Fig. S2b**). 30,33 $\cancel{1}$ Negatively charged sulfate groups (-OSO₃-) are introduced onto the CNC's surface, which promotes CNC's 1 2 dispersion by electrostatic repulsion due to the negative charge. 34 In contrast, CNC-S, obtained from the 1 treatment of wood pulp with sulfuric acid, features rod-shaped cellulose nanocrystals with an average particle 134 length of 291 \pm 24 nm and a diameter ranging below 10 nm (**Fig. S2c**). The morphology of rGO is shown in 1\frac{1}{2}5 Fig. S3, where the SEM and TEM images display a uniform surface with fewer visible wrinkles.

The above nanocelluloses were combined with GO and calcined at 600 °C to produce carbon 13/47 nanocomposites. SEM and TEM images (Fig. 1) reveal distinct structural features for each nanocellulose type within the rGO framework. The SEM images (Fig. 1a-b, e-f, and i-i) demonstrate a predominantly sheet-like morphology for all samples, with nanocellulose components blending into the rGO matrix, making it difficult to distinguish between them as only rGO sheets are visible. TEM images at both high and low magnifications illustrate significant differences in nanocellulose morphology and distribution within the rGO composites, impacting the overall structure. In the CNF/rGO composite (Fig. 1c-d), the low magnification TEM clearly reveals the CNF structure, while the high magnification shows CNF encased by thin rGO sheets. For the CNC-124 L/rGO composite (Fig. 1g-h), low magnification TEM indicates an uneven dispersion of CNC-L and rGO, 125 leading to visible voids and gaps. By contrast, the CNC-S/rGO composite (Fig. 1k-l) displays a compact 126 structure, where CNC-S particles are evenly distributed within the rGO matrix, minimizing voids or large pores.



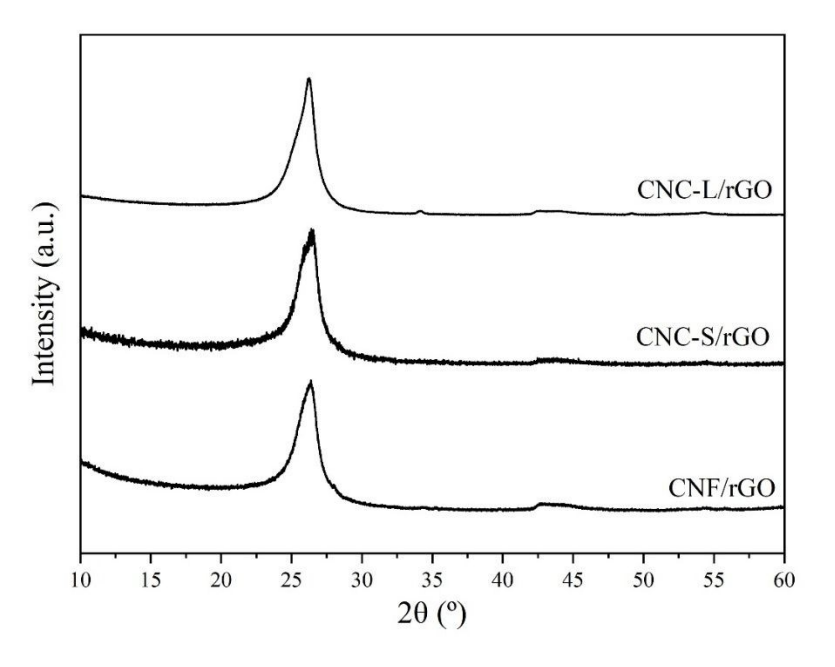
128 Fig. 1. (a, b) SEM and (c, d) TEM images of CNF/rGO nanocomposite. (e, f) SEM and (g, h) TEM images of CNC-L/rGO nanocomposite, and (i, j) SEM and (k, l) TEM images of CNC-S/rGO nanocomposite.

152025 05.17.16.

130

131

XRD analysis was conducted to investigate the crystal structure of the materials. Fig. S3c of the rGO 1\(\frac{1}{2}\)2 XRD pattern exhibits a distinct diffraction peak at $2\theta = 26.36^{\circ}$ corresponding to the (002) plane. This peak is 1\(\frac{1}{2}\)3 observed, whereas the characteristic diffraction peak of GO at approximately 11° is not present, \(^{36,37}\) indicating 1\frac{3}{2}4 the elimination of oxygen-containing functional groups and interlayer water. 38,39 Additionally, the interlayer \$\frac{1}{2}5\$ spacing (d-spacing) decreases from 0.81 nm in GO to 0.34 nm in rGO, \$\frac{36,40}{2}\$ further confirming the successful 136 conversion of GO to rGO. For the CNF/rGO, CNC-L/rGO, and CNC-S/rGO nanocomposites (Fig. 2), XRD peaks appear around $2\theta = 26.4^{\circ}$, 26.2° , and 26.4° , respectively, corresponding to the (002) plane where the 138 characteristic peaks of nanocelluloses at $2\theta = 15^{\circ}$ and 22° disappear following hybridization. ^{30,36} The observed 139 d-spacing (around 0.34 nm) in all the nanocomposites is consistent with that of rGO without nanocelluloses, 41,42 140 likely due to the relatively low nanocellulose concentration in the nanocomposite. 42

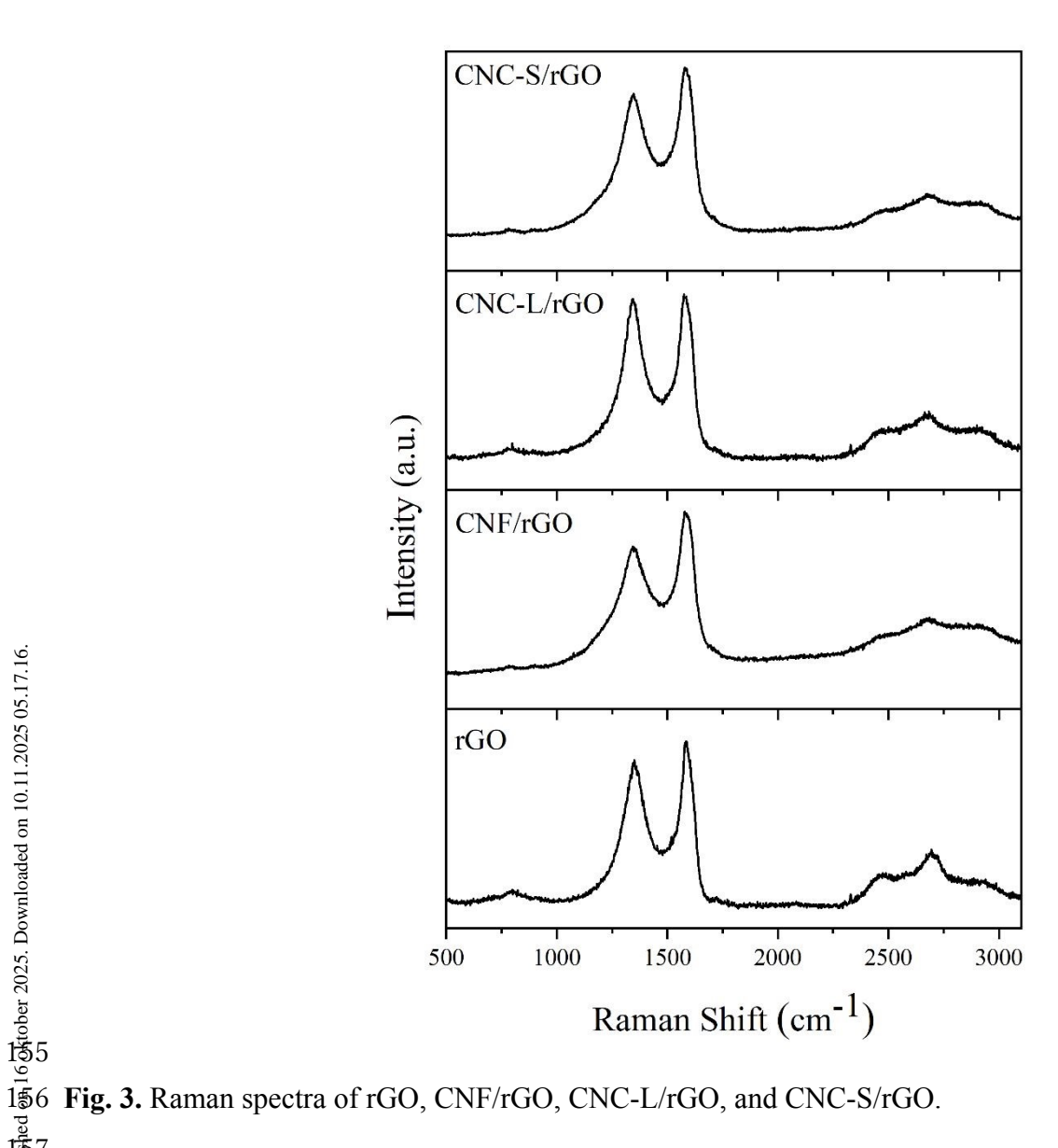


View Article Online DOI: 10.1039/D5NH00306G

142 Fig. 2. Wide-angle XRD patterns of CNF/rGO, CNC-L/rGO, and CNC-S/rGO, respectively.

Raman spectroscopy is an essential technique for determining the degree of graphitization in carbon-based materials. The number of structural defects is typically assessed by analyzing the intensity ratio of the G band, which corresponds to the graphitic structure with sp² hybridization arranged in a two-dimensional lattice, to the D band, which is associated with the presence of amorphous carbon in the sample. The D band typically arises from defects such as boundaries and edges in the carbon lattice. ⁴³ **Fig. 3** shows the G and D bands of rGO observed at 1586.4 and 1353.6 cm⁻¹, respectively. The integrated intensity ratio of the D peak to the G peak G peak G peak G in the synthesized materials, is found to be 0.90 for rGO. After hybridization with nanocellulose, the G ratios were calculated to be 0.82, 0.98, and 0.87 for CNF/rGO, CNC-G increased defects or disorders. This is attributed to the observation that CNC-L exhibits the highest degree of amorphous carbon formation during heating at high temperatures. ⁴⁴

View Article Online DOI: 10.1039/D5NH00306G



parts 7 158The thermal stability of GO, CNF/GO, CNC-L/GO, and CNC-S/GO was analyzed using 159 thermogravimetric analysis (TGA) under a nitrogen atmosphere (Fig.4). The GO (Fig. 4a) exhibits an initial 160 weight loss of approximately 12.6% below 150 °C due to absorbed water. 45,46 This is followed by a major 161 decomposition of oxygen-containing functional groups with a weight loss of 34.8% up to 880 °C, ⁴⁷ resulting in 162 a residual weight of 52.6%, which indicates the presence of thermally stable carbonaceous structures. In contrast, 163 the nanocellulose/GO nanocomposites (Fig. 4b-d) also show an initial weight loss below 150 °C related to water 164 adsorption. When carbon yields are calculated by using the weight ratios after water desorption at 150 °C (W 165 [%]) and the residual weight ratios after heating up to 880 °C (R [%]) (Carbonization degree = $W/R \times 100$ [%]), 166 CNC-L/GO exhibits a larger carbon yield (46.2%) compared to CNF/GO (36.9%) and CNC-S/GO (36.7%). The

167 relatively high carbon yield of CNC-L/GO suggests strong interactions between CNC-L and the GO matrix. 45

Downlosted of 10.11.2025 05.17.16.

179

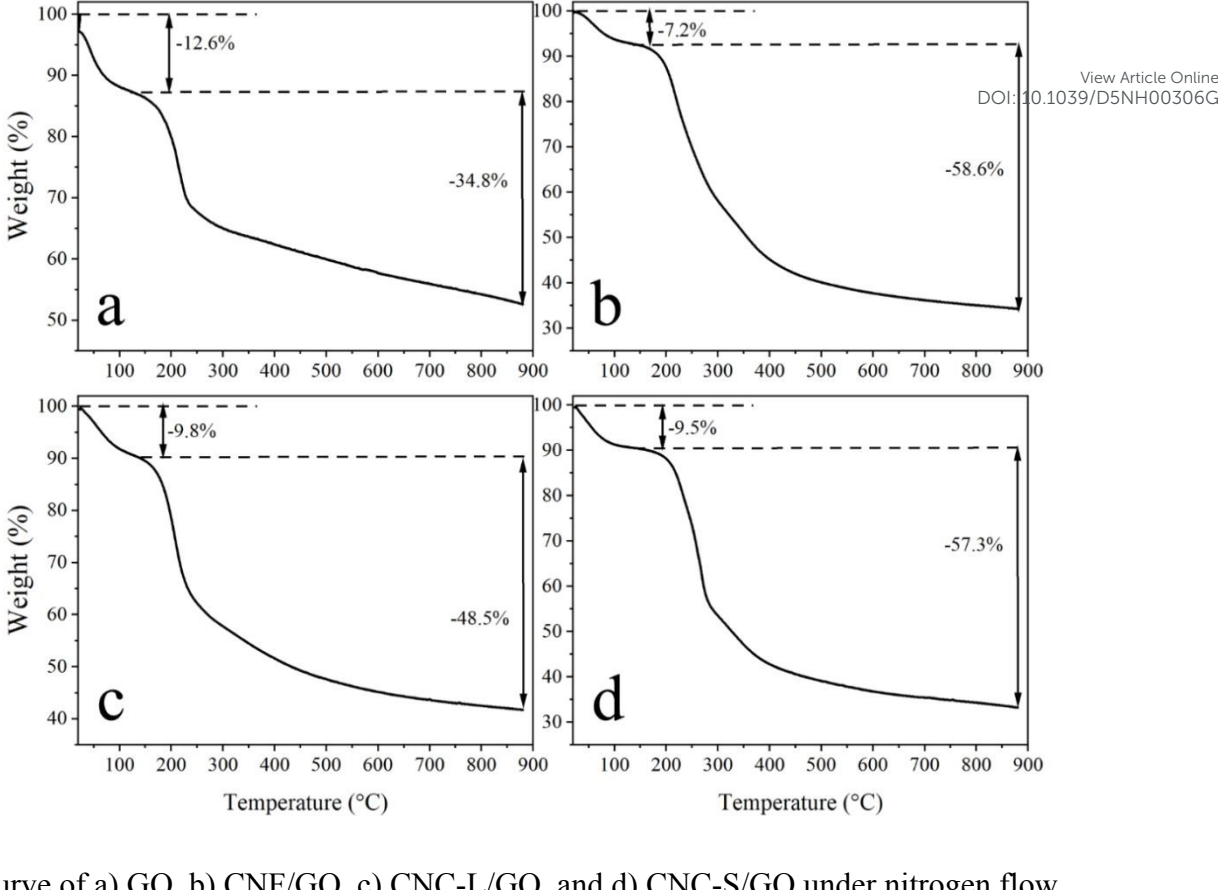


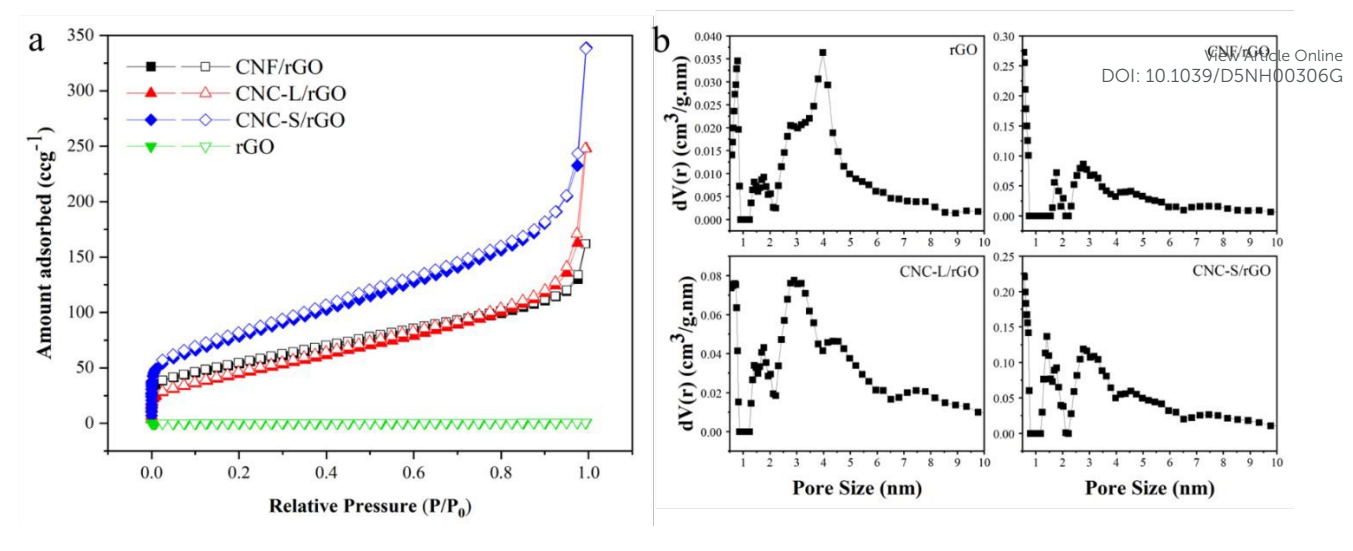
Fig. 4. TGA curve of a) GO, b) CNF/GO, c) CNC-L/GO, and d) CNC-S/GO under nitrogen flow.

The surface area and pore size distribution for all nanocellulose-derived carbon/rGO nanocomposites were assessed through nitrogen adsorption/desorption using Brunauer-Emmett-Teller (BET) analysis (Fig. 5a, 173 **Table 1**). The addition of nanocellulose significantly enhances the surface area of rGO alone (45.7 m² g⁻¹). 14 Precisely, the CNC-S/rGO nanocomposite displays the highest surface area at 283.9 m² g⁻¹, followed by CNF/rGO at 188.9 m² g⁻¹ and CNC-L/rGO at 170.6 m² g⁻¹. This increase is likely due to the small nanocellulose 176 fibers acting as spacers, which help prevent rGO sheets from restacking and maintain their separation. Fig. 5b 177 shows the pore size distributions of the samples. The distributions indicate mesopores are largely introduced by 178 hybridization.

1384

168ktober 2025. Downloaded on 10.11.2835

199



182 Fig. 5. (a) N₂ adsorption-desorption isotherms, and (b) the NLDFT pore size distribution curve of rGO. CNF/rGO, CNC-L/rGO and CNC-S/rGO, respectively.

Table 1. Surface area and pore size

Sample name	Surface area (m ² g ⁻¹)	Pore volume (cm ³ g ⁻¹)
rGO	45.7	0.05
CNF/rGO nanocomposite	188.9	0.18
CNC-L/rGO nanocomposite	170.6	0.23
CNC-S/rGO nanocomposite	283.9	0.33

Numerous studies have demonstrated that the presence of relatively large pores like mesopores is a critical factor in the design and performance of CDI materials, as it significantly influences the ability of 189 electrode materials to store and release ions. ^{48,49} CNF/rGO, CNC-L/rGO, and CNC-S/rGO, which exhibit high 190 specific surface area, large pore volume, and well-developed mesoporosity, emerge as promising candidates for 191 CDI electrodes. Notably, CNC-L/rGO incorporates longer carbon chains derived from long nanocellulose, 192 which facilitate the formation of efficient conductive pathways within the material, thereby improving its 193 electrochemical performance. Therefore, CNC-L/rGO is selected for further CDI testing compared to rGO. 194 CNC-L strengthens the rGO structure by forming strong interactions with rGO sheets. At the same time, its well-195 dispersed fibers help maintain material integrity and prevent aggregation, resulting in improved mechanical 196 stability and durability. Also, its larger pore size prevents rGO sheets from stacking too closely together, preserving a high surface area and facilitating efficient ion transport. This optimized structure enhances ion adsorption and release, which is essential for superior capacitive deionization (CDI) performance.

An asymmetric CDI configuration was constructed with rGO and CNC-L/rGO as the cathode for Na⁺ 200 capture and activated carbon (AC) as the anode for Cl⁻ capture. Compared to the symmetric CDI configuration, 201 asymmetric CDI configurations exhibit enhanced desalination performance due to several advantages. These

213

22/23

235

202 include the higher safe operation voltage (enabling operation at high voltage without inducing water splitting) 203 and greater flexibility in the choice of electrode materials for Na⁺ or Cl⁻ selectivity.

Fig. 6 illustrates the desalination performance of the samples studied at an initial NaCleon centration 205 of 500 mg L⁻¹ and operating voltage of 1.2 V, which is acceptable for asymmetric CDI cells. During the CDI 206 process, no bubbles are observed, indicating the absence of side reactions, such as chlorine generation or water splitting. As shown in Fig. 6a-b, CNC-L/rGO demonstrates a high ion adsorption capacity (IAC) for Na⁺ of 208 37.46 mg g⁻¹ and a salt adsorption capacity (SAC) of 46.82 mg g⁻¹, significantly outperforming rGO, which has 209 an IAC (Na⁺) of 6.72 mg g⁻¹ and SAC of 8.4 mg g⁻¹. Moreover, the CNC-L/rGO exhibits a higher IAR within 30 minutes (Fig. 6c). The corresponding CDI Ragone plots (Fig. 6d) show that CNC-L/rGO shifts toward the 211 upper right region, indicating higher IAC (Na⁺) and faster IAR (Na⁺) than rGO, due to large pore size and high

212 surface area, which facilitates efficient ion adsorption and transport, critical for CDI performance.

For practical applications, the feedwaters used in CDI systems often consist of brines with varying 244 concentrations. Therefore, achieving high CDI performance across a wide range of concentrations is crucial. 2d 5 The performance of CNC-L/rGO was further evaluated in NaCl solutions with concentrations ranging from 250 266 to 2000 mg L⁻¹. As the NaCl concentration increased, the Na⁺ capture capacity also increased (**Fig. 6e**). Notably, 2½7 CNC-L/rGO achieves an ultrahigh IAC (Na⁺) of 45.67 mg g⁻¹ at 2000 mg L⁻¹, along with a very high SAC of 2 57.08 mg g⁻¹ (Table S1). Long-term cycling stability is another critical criterion for assessing practical CDI performance. The CNC-L/rGO nanocomposite was evaluated for stability at 1.2 V. Fig. 6f shows that the CNC-L/rGO nanocomposite exhibits excellent cycling stability, with no significant performance degradation even after 50 cycles. To further clarify the details of electrochemical Na⁺ adsorption, ex-situ X-ray photoelectron spectroscopy (XPS) measurements were carried out on the CNC-L/rGO sample before and after Na⁺ adsorption.

As presented in Fig. S4a, the C 1s spectra of the as-prepared CNC-L/rGO electrode were deconvoluted 24 into three peaks centered at approximately 290, 286, and 285 eV, corresponding to O-C=O, C-O, and C-C/C=C 225 bonds, respectively. ⁵⁰ After Na⁺ adsorption (**Fig. S4b**), the O-C=O bond peak shifts toward lower binding energy, and the C-O bond peak shifts to higher binding energy, indicating redox activity related to these functional groups. Additionally, a new peak emerged at around 283 eV, attributable to Na-C interactions.⁵¹ These findings align well with previously reported behaviors of sodium-ion interactions during charge/discharge processes. 52 Even after the CDI test, in the Raman spectra (Fig. S5a), the I_D/I_G ratio after CDI measurement 230 remains almost unchanged (0.97), indicating that the defect density and graphitic ordering of the carbon framework are preserved during the cycling. This suggests that the conductive network remains intact under 232 operating conditions. The wide-angle XRD results (Fig. S5b) further confirm the structural robustness of the 233 material. Even after the CDI measurement, the (002) peak is still observed at 26.4°, with the calculated d-space 234 remaining at 0.34nm.

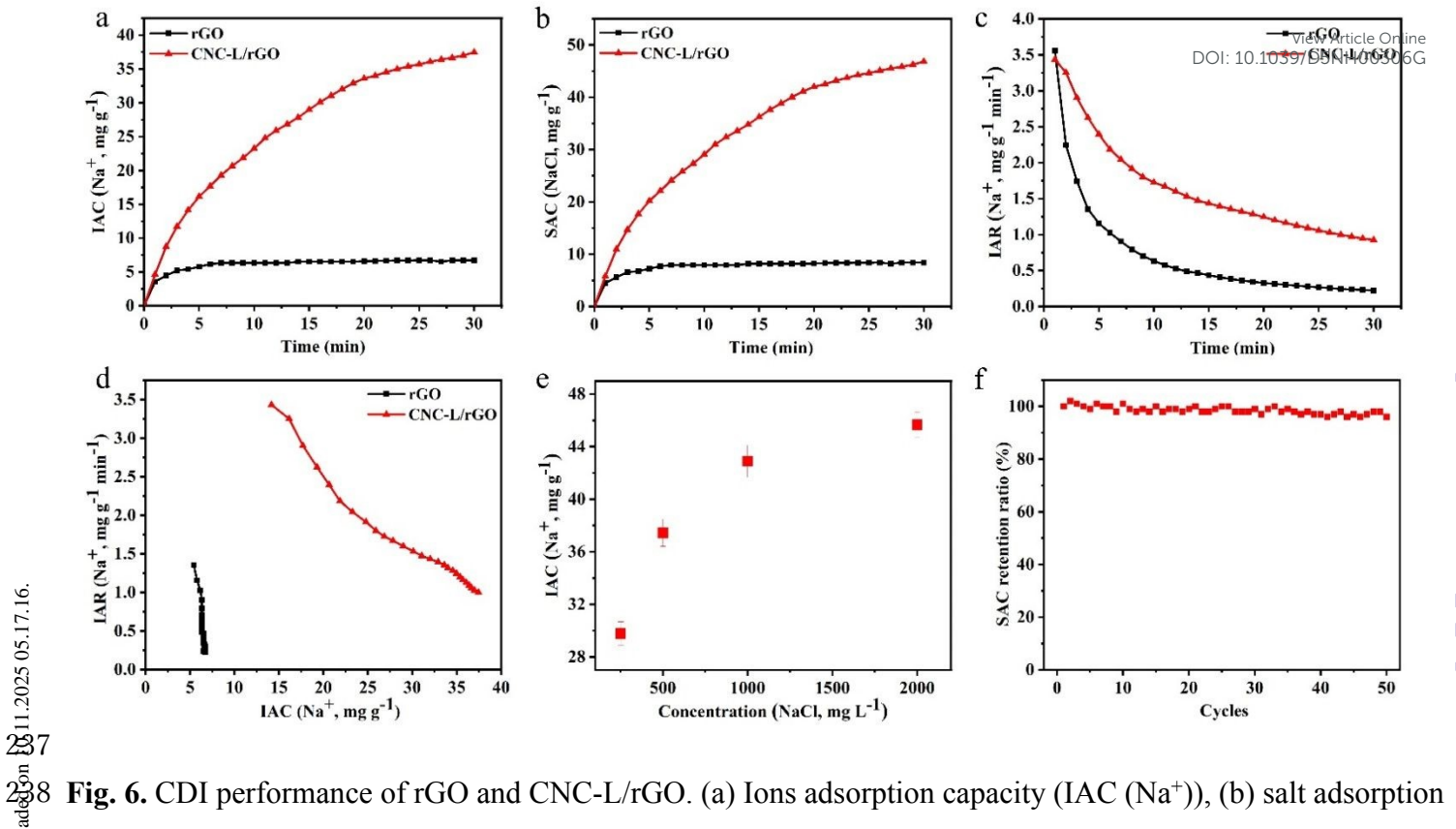


Fig. 6. CDI performance of rGO and CNC-L/rGO. (a) Ions adsorption capacity (IAC (Na⁺)), (b) salt adsorption capacity (SAC (NaCl)), (c) ions adsorption rate (IAR (Na⁺)) of the materials in 500 mg L⁻¹ NaCl solution at 1.2 V, and (d) the corresponding Ragone plots for the materials in 500 mg L⁻¹ NaCl solution at 1.2 V. (e) Sodium chloride concentration dependency of CDI performance for CNC-L/rGO at 1.2 V, (f) Long-term cycling stability test of CNC-L/rGO in 500 mg L⁻¹ NaCl solution at 1.2 V.

24 4. Conclusions

243

253

In summary, this study has successfully demonstrated nanocellulose-derived carbon/rGO nanocomposites using three distinct nanocellulose morphologies (CNF, CNC-L, and CNC-S), achieving enhanced surface areas exceeding between 170 and 283.9 m² g⁻¹ due to the nanocellulose's role as a spacer preventing rGO restacking. CNC-L/rGO nanocomposite has demonstrated superior CDI performance, achieving a high IAC of 45.67 mg g⁻¹ for Na⁺ and an SAC of 57.08 mg g⁻¹ at a NaCl concentration of 2000 mg L⁻¹. It also demonstrates excellent adaptability across saline concentrations (250–2000 mg L⁻¹ NaCl) and long-term cycling stability over 50 cycles. These results highlight nanocellulose-derived carbon/rGO nanocomposite as a promising, scalable CDI material for efficient water desalination, paving the way for tailored designs to enhance desalination performance further.

254 Acknowledgements

This research was financially supported by the JST ERATO Yamauchi Materials Space-Tectonics Project (JPMJER2003). Additionally, a portion of this work was conducted at the Queensland node of the Australian National Fabrication Facility, an organization established under the National Collaborative Research Infrastructure Strategy to provide nano- and microfabrication facilities for researchers across Australia. We also

259 express our gratitude to English editing tools such as ChatGPT, Grammarly, and others, which assisted us in 260 identifying and correcting grammatical errors in our manuscript.

> View Article Online DOI: 10.1039/D5NH00306G

262 Experimental Section

- 263 Preparation of nanocellulose-derived carbon/rGO nanocomposites: Equal volumes of the above-prepared
- 264 GO suspension and nanocellulose suspension (CNF, CNC-L, and CNC-S) were separately stirred in individual
- 265 beakers. The GO suspension was then gradually added to the nanocellulose suspension under continuous stirring
- 266 to form a binary suspension, with stirring maintained for an additional 20 minutes. The binary suspension was
- 267 sonicated for 30 minutes and stirred magnetically for 24 hours. After these preparatory steps, the binary
- 268 suspension was freeze-dried to obtain a dry nanocellulose/GO nanocomposite. This composite was then
- 269 carbonized in a tube furnace at 600 °C for 8 hours with a temperature ramp of 5 °C min⁻¹ under a nitrogen
- 270 atmosphere to produce the nanocellulose-derived carbon/rGO nanocomposites. Once cooled to room
- 251 temperature, the carbonized product was removed from the furnace and stored for subsequent use. The resulting
- 2\(2\) samples were abbreviated as CNF/rGO, CNC-L/rGO, and CNC-S/rGO nanocomposites. For comparison,
- 273 pristing rGO was prepared directly from GO under identical conditions without the addition of nanocellulose.

2 Reference:

- T. Lu, Y. Liu, X. Xu, L. Pan, A.A. Alothman, J. Shapter, Y. Wang and Y. Yamauchi, Sep. Purif. Technol. 2/7
 - 2021, **256**, 117771.
- 2 8 2 Q. Li, X. Xu, J. Guo, J.P. Hill, H. Xu, L. Xiang, C. Li, Y. Yamauchi and Y. Mai, Angew. Chem. Int. Ed.,
- $2\bar{2}9$ 2021, **60**, 26528–26534.
- $2\sqrt[5]{8}0$ 3 M.A. Anderson, A.L. Cudero and J. Palma, *Electrochim. Acta*, 2010, 55, 3845–3856.
- S. Dutta, S.-Y. Huang, C. Chen, J. E. Chen, Z. A. Alothman, Y. Yamauchi, C.-H. Hou, K. C.-W. Wu, ACS **2**81 4
- 282 Sustainable Chem. Eng., 2016, 4, 1885-1893.
- 283 5 M. Elimelech and W.A. Phillip, *Science*, 2011, **333**, 712–717.
- R.F. Service, Science, 2006, 313, 1088–1090. 284 6
- H. Deng, Z. Wang, M. Kim, Y. Yamauchi, S.J. Eichhorn, M.M. Titirici and L. Deng, *Nano Energy*, 2023. 285 7
- **117**, 108914. 286
- C.L. Yeh, H.C. Hsi, K.C. Li and C.H. Hou, *Desalination*, 2015, **367**, 60–68. 287 8
- S. Hu, D. Fang, F.Li, Z. Xu, K. Li, P.Zhang, W. Feng, Desalination, 2025, 601, 118608. 288 9
- D. Jiang, J. P. Hill, J. Henzie, H. N. Nam, Q. M. Phung, L. Zhu, J. Wang, W. Xia, Y. Zhao, Y. Kang, T. Asahi, 289 10
- R. Bu, X. Xu and Y. Yamauchi, J. Am. Chem. Soc., 2025, 147, 12460–12468. 290
- Y. Li, Y. Wang, Y. Cai, R. Fang, L. Zhang, Desalination, 2024, 577, 117387. 291 11
- X. Xu, S. Zhang, J. Tang, L. Pan, M. Eguchi, J. Na, Y. Yamauchi, EnergyChem, 2020, 2, 100043. 292 12
- K. Laxman, L. Al Gharibi and J. Dutta, *Electrochim. Acta*, 2015, 176, 420–425. 293 13
- H. Wang, B. Chen, D.J. Liu, X. Xu, L. Osmieri and Y. Yamauchi, *Small*, 2022, **18**, 2102477. 294 14
- Q. Liu, S. Bi, X. Xu, X. Xiao and Y. Lei, J. Colloid Interface Sci., 2025, 680, 54-63.

- 296 16 H. M. Saif, B. Ferrández-Gómez, V. D. Alves, R. M. Huertas, G. Alemany-Molina, A. Viegas, E. Morallón,
- D. Cazorla-Amorós, J. G. Crespo, S. Pawlowski, *Desalination*, 2025, **602**, 118638.
- 298 17 Z. Liu, B. Wei, K. Liu, L. Wang, Sep. Purif. Technol., 2024, 345, 127380.
- DOI: 10.1039/D5NH00306G

View Article Online

- 299 18 S. Zhang, Z. Ye, M. Ma, P. Yin, Y. Bao, F. Li, Desalination, 2025, 603, 118679.
- 300 19 R. Patil, D. Jiang, X. Xu, N. Kumar, S. Bhattacharjee, S. K. Yadav, D. Kalyanasundaram, R. R Salunkhe,
- 301 A. Bhaumik, N. Khaorapapong, Y. Yamauchi, S. Dutta, *Chem. Eng. J.*, 2025, **506**, 159270.
- 302 20 C. Santos, E. García-Quismondo, J. Palma, M.A. Anderson and J.J. Lado, *Electrochim. Acta*, 2020, 330,
- 303 135216.
- 304 21 H. Zhang, F. Zhang, Y. Wei, Q. Miao, A. Li, Y. Zhao, Y. Yuan, N. Jin and G. Li, ACS Appl. Mater.
- 305 *Interfaces*, 2021, **13**, 21217–21230.
- 306 22 A. Ahmed, B. Adak, M.O. Faruk and S. Mukhopadhyay, *Ind. Eng. Chem. Res.*, 2021, 60, 10882–10916.
- 307 23 H. Yang, H. Zheng, Y. Duan, T. Xu, H. Xie, H. Du and C. Si, Int. J. Biol. Macromol., 2023, 253, 126903.
- 3298 24 A. Brakat and H. Zhu, Nano-Micro Lett., 2021, 13, 94.
- 369 25 J. Xing, P. Tao, Z. Wu, C. Xing, X. Liao and S. Nie, Carbohydr. Polym., 2019, 207, 447–459.
- **3**10 26 A. Brakat and H. Zhu, ACS Appl. Bio Mater., 2021, **4**, 7366–7401.
- 31 27 S. Dutta, S.-Y. Huang, C. Chen, J. E. Chen, Z. A. Alothman, Y. Yamauchi, C.-H. Hou and K. C.-W. Wu
- 3\frac{3}{2} 2 ACS Sustain Chem Eng, 2016, 4, 1885–1893.
- 3 28 D. Lin, Z. Zhou, R. Shi, B. Chen, Z. Huang, H. Tang, J. Wang, X. Zhu, C. Shao and F. Han, J Mater Chem
- 3 4 *A Mater*, 2024, **12**, 19885–19890.
- 35 29 M. Tauk, G. Folaranmi, M. Cretin, M. Bechelany, P. Sistat, C. Zhang and F. Zaviska, *Elsevier Ltd*, 2023,
- 3\frac{3}{2}6 preprint, DOI: 10.1016/j.jece.2023.111368.
- 3 7 30 N. Amiralian, M. Mustapic, M.S.A. Hossain, C. Wang, M. Konarova, J. Tang, J. Na, A. Khan and A.
- 類8 Rowan, J. Hazard. Mater., 2020, **394**, 122571.
- 319 31 M.L. Pitcher, R. Koshani and A. Sheikhi, *J. Polym. Sci.*, 2024, **62**, 9–31.
- 320 32 G. Ramezani, T. G. M. van de Ven, I. Stihara, Recent prog. mater., 2025, 7, 1-50.
- 321 33 N. Amiralian, P.K. Annamalai, C.J. Garvey, E. Jiang, P. Memmott and D.J. Martin, Cellulose, 2017, 24,
- 322 3753–3766.
- 323 34 F.V. Ferreira, M. Mariano, S.C. Rabelo, R.F. Gouveia and L.M.F. Lona, Appl. Surf. Sci., 2018, 436, 1113–
- 324 1122.
- 325 35 R.J. Moon, A. Martini, J. Nairn, J. Simonsen and J. Youngblood, *Chem. Soc. Rev.*, 2011, **40**, 3941–3994.
- 326 36 K. Ge, H. Shao, E. Raymundo-Piñero, P.L. Taberna and P. Simon, Nat. Commun., 2024, 15, 1935.
- 327 37 M. A. Farea, N. Yusof, H. Y. Mohammed, M.N. Murshed, M.E. Al Sayed, D. Abdehameed, Mater Sci
- 328 *Semicond Process*, 2025, **188**, 109219.
- 329 38 Y. Song, H. Lee, J. Ko, J. Ryu, M. Kim and D. Sohn, *Bull. Korean Chem. Soc.*, 2014, **35**, 2009–2012.
- 330 39 Abid, P. Sehrawat, S.S. Islam, P. Mishra and S. Ahmad, Sci. Rep., 2018, 8, 3537.
- 331 40 V. Paranthaman, K. Sundaramoorthy, B. Chandra, S.P. Muthu, P. Alagarsamy and R. Perumalsamy, Phys.
- 332 Status Solidi A, 2018, **215**, 1800298.

- 333 41 I. Ahmed, R. Biswas, R. Sharma, V. Burman and K.K. Haldar, Front. Chem., 2023, 11, 1129133.
- 334 42 L. Zhu, Y. Cao, B. Jiang, J. Yu, J. Zhu and Z. Hu, J. Alloys Compd., 2023, **969**, 172117.
- 335 43 D. López-Díaz, J.A. Delgado-Notario, V. Clericò, E. Diez, M.D. Merchán and M.M. Velázquez, Courtings,
- 336 2020, **10**, 524.
- 337 44 H. Liu, T. Xu, C. Cai, K. Liu, W. Liu, M. Zhang, H. Du, C. Si and K. Zhang, Adv. Funct. Mater., 2022, 32,
- 338 2113082.
- 339 45 V.T. Nguyen, L.Q. Ha, T.D.L. Nguyen, P.H. Ly, D.M. Nguyen and D. Hoang, ACS Omega, 2022, 7, 1003–
- 340 1013.
- 341 46 F. D'Acierno, W.Y. Hamad, C.A. Michal and M.J. Maclachlan, Biomacromolecules, 2020, 21, 3374–3386
- 342 47 M. Karakoti, R. Jangra, S. Pandey, P.S. Dhapola, S. Dhali, S. Mahendia, P.K. Singh and N.G. Sahoo, High
- 343 Perform. Polym., 2020, 32, 175–182.
- 344 48 X. Sun, Z. Hao, X. Zhou, J. Chen and Y. Zhang, *Chemosphere*, 2024, **346**, 140601.
- 345 49 K. Sun, M. Tebyetekerwa, C. Wang, X. Wang, X. Zhang and X.S. Zhao, *Adv. Funct. Mater.*, 2023, **33**, 2213578.
- 347 50 R. Shu, L. Xu, Y. Guan, J. Colloid Interface Sci., 2024, 675, 401-410.
- S. Aina, B. Tratnik, A. Vizintin, E. Tchernychova, M. P. Lobera, R. Dominko, M. Bernechea, *J. Power Sources*, 2024, **610**, 234730.
- D. Jiang, R. Xu, L. Bai, J. P. Hill, L. Zhu, W. Xia, R. Bu, Y. Zhao, Y. Kang, T. Hamada, R. Ma, N. Torad, J. Wang, T. Asahi, X. Xu, Y. Yamauchi, Adv. Funct. Mater., 2024, 34, 24079.

View Article Online DOI: 10.1039/D5NH00306G

Data availability

Data supporting this study are included within the article and/or ESI.